Title
Parametric Model Identification of Axisymmetric MEMS Resonators

Journal
Journal of Microelectromechanical Systems, 30(2)

ISSN
1057-7157

Authors
Schein, Stephen
M'Closkey, Robert T

Publication Date
2021-04-01

DOI
10.1109/jmems.2020.3043660

Peer reviewed

Parametric model identification of axisymmetric MEMS resonators

Stephen Schein and Robert M'Closkey

***Abstract*—This paper proposes a technique for developing parametric models of modally degenerate resonators from stimulus-response data. The technique complements traditional empirical frequency response estimates that are commonly used for testing MEMS resonators, however, the parametric models have distinct advantages when the modal frequency differences are close enough to frustrate estimates of quality factors, natural frequencies and mode orientations. The proposed technique also completely rejects parasitic coupling between the stimulus and pick-off electrodes. It is shown how a modification of the algorithm using demodulated measurement signals greatly reduces storage and computational requirements.**

I. Introduction

Identifying the modal properties of axisymmetric resonators presents unique challenges as a consequence of nearly identical modal frequencies appearing within clusters of degenerate modes. This paper presents a testing and modeling technique to identify parametric models of resonators from which modal frequencies, time constants and mode orientations can be determined. The proposed technique is particularly suited for studying modally degenerate resonators because the multi-input/multi-output stimulus-response data that are required for accurately identifying degenerate modes is effortlessly handled within the proposed modeling framework. Although knowledge of modal frequencies and time constants is typically the objective of MEMS resonator testing, mode orientations are also of interest because they feature in various "tuning" algorithms that attempt to eliminate frequency differences in degenerate mode resonators. For example, tuning algorithms for generic thin ring resonators using mass deposition are proposed in [1–3]. Identification of the mode orientations was central to successful tuning in these references. These algorithms were adapted for practical application in an axisymmetric MEMS resonator to permanently eliminate detuning in the "wine glass" pair of modes [4, 5]. The proposed modeling technique also rejects parasitic, or feedthrough, coupling between the electrodes used to stimulate the resonator and the electrodes used as signal pick-offs. Thus, the transfer function that is produced only models the electromechanical components contributing to resonator motion.

Non-parametric frequency response methods based on FFT processing of input-output data records are undoubtedly the workhorse modeling tools in MEMS resonator testing. Many instruments and analyzers feature built-in functions that automate the data collection and signal processing to produce empirical frequency response estimates. Modal frequencies and damping (quality factor) can be directly estimated from graphical representations or, alternatively, parametric models can be fit to the frequency response data using curve fitting techniques and then the modal parameters can be extracted from the models, e.g., [6] is an early reference describing an iterative least squares algorithm to fit a rational transfer function to empirical frequency response data; [7] describes an implementation in a modern signal analyzer. With regard to modeling MEMS, [8] considers a parametric model consisting of a resonator in series with a capacitor that is fit to frequency response data in order to identify motional and parasitic components, and [9] demonstrates a technique for estimating the frequency response of a single degree-of-freedom resonator by fitting a sinusoidal time function to the periodic response under periodic pulse forcing –the pulse couples to the measurements due to parasitics but the corrupted segments are removed from the time-domain data prior to fitting the sinusoid. Second order models parameterized by mass, stiffness, and damping matrices are fit to multi-input/multi-output frequency response data in [10, 11] for modeling two degree-of-freedom (2-DOF) resonators.

Alternative signal processing techniques can be directly applied to the measurement data. Principal component analysis is used to analyze correlations of free response measurements obtained from a 2-DOF resonator to estimate stiffness anisotropy in [12]. Non-parametric spectral estimation is applied to resonator thermal noise measurements in [13] to determine modal frequencies and quality factors with reduced biases compared what is typically achieved with windowed data records. An adaptive filter for cancelling parasitic feedthrough is proposed in [14]; the frequency response of the resonator is subsequently identified from the feedthrough-compensated data. Auto-regressive models are fit to input-output data from a 2-DOF resonator in [15] in order to extract mode orientations.

High quality factor resonators can present challenges for traditional frequency response testing techniques due to the high dynamic range of the resonator response as a function of frequency, frequency resolution (grid spacing), and settling times. Thus, measurements from transient "ring-down" data have gained prominence for estimating modal frequencies and time constants, the latter of which can be determined from the transient decay envelope, e.g., [16–20]. Transient response measurements are robust and straightforward to implement when modes are sufficiently separated, however, care is required when the modes are nearly degenerate (small detuning)

The authors are with the Mechanical and Aerospace Engineering Department, University of California, Los Angeles, CA 90095 USA.

Stephen Schein is a Graduate Student Researcher. Robert M'Closkey is a Professor and the corresponding author, (310) 825-2909, rtm@seas.ucla.edu.

because it is difficult to selectively excite only one mode in this case. Thus, the precise positioning or blending of pick-offs, often performed iteratively, is necessary to isolate the response of a single resonant mode.

The proposed modeling technique is complementary to the aforementioned methods and yields detailed information on a resonator's model properties even when the frequency detuning is effectively zero. The only requirement is that there are enough excitation and pick-off electrodes to couple to each mode of interest. Although this requirement appears to rely on knowledge of the mode shapes, it is possible to define an electrode layout that will achieve the desired coupling in all circumstances and, hence, *a priori* knowledge of the modes, other than their general location in frequency, is not necessary. The proposed technique, which can be viewed as an extension of transient ring-down modeling, produces a linear model. This is no different than the majority of methods reviewed above because they either implicitly or explicitly assume a linear system is generating the data, i.e. Lorentzian frequency response magnitude, exponential decay envelopes and so forth.

The paper is organized as follows. Sec. II briefly reviews the Ho-Kalman algorithm for identifying linear models from pulse response data. Sec. III adapts the Ho-Kalman algorithm for identifying the $n = 1, 2, 3$ pairs of modes in an axisymmetric MEMS resonator. The modeling results are presented and discussed in Secs. IV and V. A "zoom" variation of the proposed method is presented in Sec. VI. The zoom method yields the same modal parameter identification results, however, the computation requirements are significantly reduced. Section VII concludes the paper.

II. Ho-Kalman prodedure

Consider a system modeled by a linear difference equation

$$\begin{aligned} \vec{x}_{k+1} &= A\vec{x}_k + B\vec{u}_k \\ \vec{y}_k &= C\vec{x}_k \end{aligned} \tag{1}$$

where $\vec{y}$ represents the pick-off measurements in response to the applied stimulus $\vec{u}$. The integer subscript k represents the sample number for the state and input and output variables. It is assumed that the sample period, denoted t_s, is uniform. There are n_i input channels, n_o output channels, and state dimension n_s. Such models arise when testing linear systems according to the block diagram in Fig. 1, where H_s, H_a and H_sys represent smoothing filters, anti-alias filters, and the system under test, respectively. The DAC implements a zero-order hold on the discrete-time signal $\vec{u}$ and the ADC samples the continuous-time signals to yield the discrete-time signal $\vec{y}$. If all dynamic elements in the block diagram are linear, then a discrete-time model of the form (1) describes the relationship between the input-output samples and the state variable $\vec{x}$, e.g., [21]. The state variables include those of the system, smoothing filters and anti-alias filters. The models are often denoted with the triplet $\{A, B, C\}$.

The foundation of the identification method proposed in this paper is the Ho-Kalman algorithm [22]. The Ho-Kalman algorithm estimates $\{A, B, C\}$ based on the pulse response of the system. The pulse response is the matrix-valued sequence

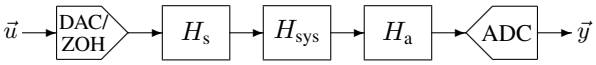

Fig. 1: Block diagram for generating test data. The system under test, anti-alias filter, and smoothing filter are denoted H_sys, H_a, and H_s, respectively.

$\{Y_k\}$, $Y_k \in \mathbb{R}^{n_\mathrm{o} \times n_\mathrm{i}}$, where $Y_0 = 0$, $Y_k = CA^{k-1}B$, $k > 0$. $\mathbb{R}$ denotes the field of real numbers. The pulse response is generated by stimulating the system, starting from a state of rest ($\vec{x}_0 = 0$), to unit pulses that are sequentially applied to each of the n_i input channels. In other words, the l^{th} column of the pulse response represents the sequence of output vectors that are obtained when the l^{th} input channel is a unit pulse and all other input channels are zero. A realization of the system is obtained by analyzing the following block-Hankel matrices formed from the pulse response data,

$$\begin{aligned} \mathcal{H}_0 &= \begin{bmatrix} Y_1 & Y_2 & \cdots & Y_{n_c} \\ Y_2 & Y_3 & \cdots & Y_{n_c+1} \\ Y_3 & Y_4 & & \vdots \\ \vdots & \vdots & \ddots & \vdots \\ Y_{n_r} & Y_{n_r+1} & \cdots & Y_{n_r+n_c-1} \end{bmatrix} \\ \mathcal{H}_1 &= \begin{bmatrix} Y_2 & Y_3 & \cdots & Y_{n_c+1} \\ Y_3 & Y_4 & \cdots & Y_{n_c+2} \\ Y_4 & Y_5 & & \vdots \\ \vdots & \vdots & \ddots & \vdots \\ Y_{n_r+1} & Y_{n_r+2} & \cdots & Y_{n_r+n_c} \end{bmatrix}, \end{aligned} \tag{2}$$

where $\mathcal{H}_0, \mathcal{H}_1 \in \mathbb{R}^{n_\mathrm{o} n_r \times n_\mathrm{i} n_c}$. The column and row dimensions use n_c and n_r pulse response samples, respectively. The number of samples that are used to create these matrices is based on the expected model order as well as the need to accurately capture time constants associated with the decay rates. Based on the model generating the pulse response data, $\mathcal{H}_0$ is factored as a product,

$$\mathcal{H}_0 = \mathcal{O}\mathcal{C}, \tag{3}$$

where $\mathcal{O}$ and $\mathcal{C}$ are the observability and controllability matrices associated with the realization,

$$\begin{aligned} \mathcal{O} &= \begin{bmatrix} C \\ CA \\ CA^2 \\ \vdots \\ CA^{n_r-1} \end{bmatrix} \in \mathbb{R}^{n_\mathrm{o} n_r \times n_\mathrm{s}}, \\ \mathcal{C} &= \begin{bmatrix} B & AB & A^2B & \cdots & A^{n_c-1}B \end{bmatrix} \in \mathbb{R}^{n_\mathrm{s} \times n_\mathrm{i} n_c}. \end{aligned} \tag{4}$$

If (1) is minimal, then the factorization shows that $\operatorname{rank}\mathcal{H}_0 = \operatorname{rank}\mathcal{O} = \operatorname{rank}\mathcal{C} = n_\mathrm{s}$ (the state dimension) when a sufficiently large number of pulse response points are used in forming $\mathcal{H}_0$ (typically, $n_\mathrm{o} n_r >> n_\mathrm{s}$ and $n_\mathrm{i} n_c >> n_\mathrm{s}$). In this manner C and B are obtained from $\mathcal{O}$ and $\mathcal{C}$, and since $\mathcal{H}_1 = \mathcal{O}A\mathcal{C}$, A is computed

$$A = \mathcal{O}^\dagger \mathcal{H}_1 \mathcal{C}^\dagger, \tag{5}$$

where $\mathcal{O}^\dagger$ and $\mathcal{C}^\dagger$ represent left and right inverses of $\mathcal{O}$ and $\mathcal{C}$, respectively, i.e. $\mathcal{O}^\dagger\mathcal{O} = I$ and $\mathcal{C}\mathcal{C}^\dagger = I$, where I denotes the identity matrix.

In practice, a model of a to-be-determined order is extracted from pulse response measurements obtained in an experiment. In this case, $\mathcal{H}_0$ and $\mathcal{H}_1$ are still formed from the samples of the transient response. The measurement samples include buffer noise and effects of disturbances and consequently $\mathcal{H}_0$ is typically full rank, however, there are often a handful of dominant singular values that can be used to closely approximate $\mathcal{H}_0$ with a lower rank matrix that is then factored according to (3). Thus, the first step in analyzing $\mathcal{H}_0$ is to compute its singular values where the number of dominant singular values provides insight into an adequate model order. Suppose $U\Sigma V^T$ is a singular value decomposition (SVD) of $\mathcal{H}_0$, where U and V are orthogonal matrices, and $(\cdot)^T$ denotes transpose. If the first r singular values of $\mathcal{H}_0$ are dominant, i.e. $\sigma_r >> \sigma_{r+1}$, then $\mathcal{H}_0$ can be approximated by a rank r matrix $\mathcal{H}_{0,r} = U_r\Sigma_r V_r^T$ where U_r is a sub-matrix of U formed from its first r columns, V_r is a sub-matrix of V formed from its first r columns, and Σ_r is a diagonal matrix with diagonal elements $\{\sigma_1, \sigma_2, \ldots, \sigma_r\}$ (the first r singular values). Thus, $\mathcal{H}_0$ is replaced by a lower rank approximation which retains the dominant singular values and the corresponding left and right singular vectors. This approach was first proposed in [23] as a variant of the basic Ho-Kalman algorithm. The results in this paper demonstrate that this approximation of $\mathcal{H}_0$ works quite well when the signal-to-noise ratio associated with the measurements is high. The factorization of $\mathcal{H}_{0,r}$ is not unique, however, other factorizations correspond to different coordinate representations of an r-state realization with the same input-output behavior. One choice of factorization based on the SVD is $\mathcal{O} = U_r\Sigma_r^{\frac{1}{2}}$ and $\mathcal{C} = \Sigma_r^{\frac{1}{2}}V_r^T$. The state space C matrix is defined as the first n_o rows of $\mathcal{O}$, and B is defined as the first n_i columns of $\mathcal{C}$. The left and right inverses of the factors are $\mathcal{O}^\dagger = \Sigma_r^{-\frac{1}{2}}U_r^T$ and $\mathcal{C}^\dagger = V_r\Sigma_r^{-\frac{1}{2}}$ and the computation of A is given by (5).

III. Application to Resonators

A. Resonator description

The modeling approach proposed in this section can be applied to any MEMS resonator, however, the Ho-Kalman procedure will be adapted for determining models of the resonator schematic shown in Fig. 2. This resonator has features that are generic to modally degenerate resonators commonly proposed for MEMS Coriolis vibratory gyros. Details on its design, fabrication, and modal properties are given in [4]. The pick-off electrodes are denoted S_1 through S_8 and the input electrodes are denoted D_1 and D_2 in Fig. 2. Thus, the input and output electrode arrangement defines a 2-input, 8-output system ($n_o = 8$ and $n_i = 2$ in (1)). A potential, denoted V_{bias}, is applied to the "Bias" electrodes to perturb the dynamics of the resonator in certain experiments. The resonator is tested in a vacuum bell jar at an approximate pressure of 100 μTorr. There is no thermal regulation of the resonator. Some heating of the resonator occurs because the electrode buffer board is colocated with the resonator inside the vacuum chamber. A thirty minute warm-up period is allotted for the pressure and temperature to roughly stabilize. The resonator die is suspended from wire bonds which are attached to the buffer board and to the die's bond pads.

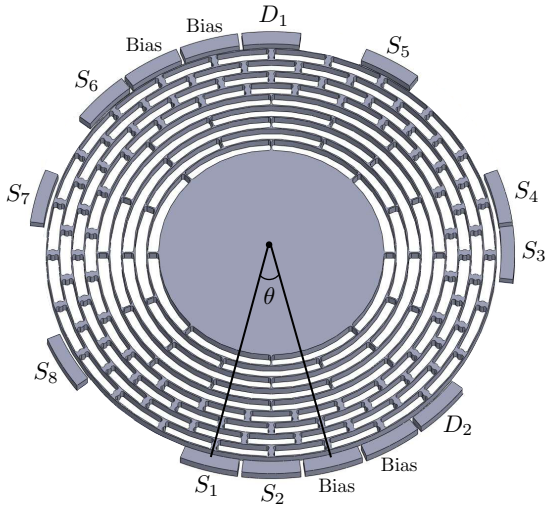

Fig. 2: Ring resonator used in tests. The resonator is 1 cm in diameter with 24 peripheral electrodes (only those electrodes used in the tests are shown). Two electrodes, denoted D_1 and D_2, are configured as input channels, and eight electrodes, denoted S_1 through S_8, are configured as pickoffs. The electrodes labeled "Bias" are used to perturb the resonator dynamics by applying a potential V_{bias} relative to the resonator bias voltage. Unused electrodes (not shown) are grounded.

The axisymmetry of the resonator imparts modal degeneracy to the $n = 1, 2, 3$ pairs of modes where the "n^{th}" pair indicates the two modes whose radial displacements are expressed to first order as $\alpha \cos n\theta + \beta \sin n\theta$, for some α, β, where θ is the angle parameter in the figure. Although the *relative* orientation of the modes within the n^{th} pair very closely subtend $90°/n$ for ring-type resonators [2], their absolute orientations with respect to the excitation and pick-off electrodes are not *a priori* known. Thus, multiple inputs and pick-offs are generally required to guarantee coupling to each mode with the relative orientation of the modes dictating the optimal electrode arrangement. The excitation electrode arrangement in Fig. 2 is ideal for exciting the $n = 2$ pair, however, these electrodes also collectively couple to the $n = 1, 3$ pairs. Furthermore, the pick-off electrode arrangement not only (collectively) detects each mode in the $n = 1, 2, 3$ pairs, it also has enough spatial resolution to accurately determine the orientation of the modes.

The frequency response derived from a broadband stimulus of the resonator is shown in Fig. 3 and serves to illustrate the general location of the $n = 1, 2, 3$ pairs of modes near 6 kHz, 14 kHz and 24 kHz, respectively. Although it is a relatively simple task to locate the modal frequencies to within a few Hz, this paper shows how to extract detailed information on the modal frequencies, damping and mode orientations even when the frequencies within a given pair are essentially equal.

B. Transient Response Data

Models are separately developed for each pair of modes. The Ho-Kalman procedure is applied to measurements of the resonator's transient, unforced response. The input is not impulsive, however, because the energy density of a pulse is

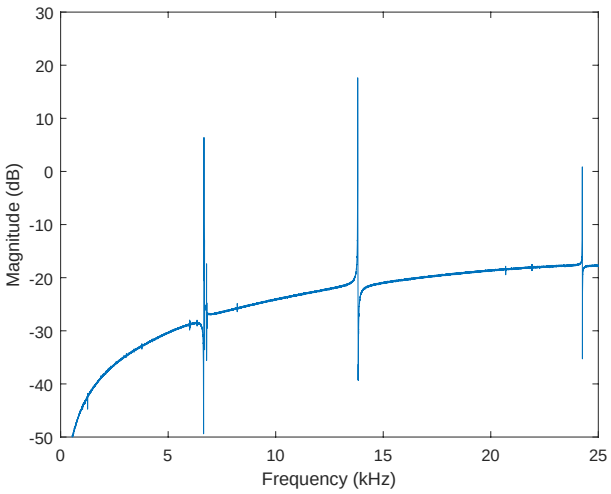

Fig. 3: Broadband frequency response of the resonator obtained from one stimulus-pick-off electrode pair. The $n = 1, 2, 3$ pairs of modes are evident.

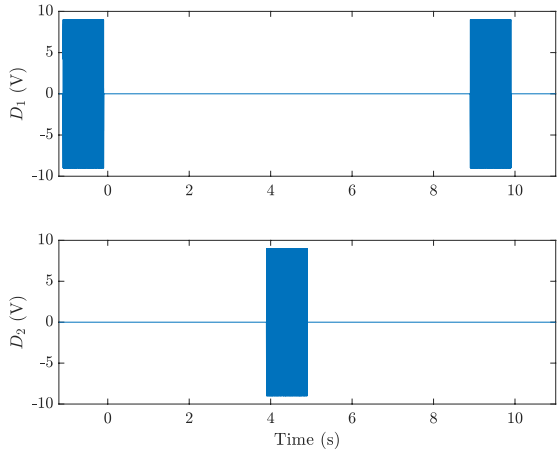

Fig. 4: Burst chirp input (8) applied to the electrodes D_1 and D_2. The signals in each input channel are periodic ($\tau_p = 10$ seconds) and have identical bursts of duration $\tau_b = 1$ second, however, there is a 5 second delay ($\tau_p/2$) between the input channels. The interval between bursts generates input-free transient data from which the resonator model is developed.

too small to evoke a measurable response due to physical limits on the pulse amplitude. Although it is possible to estimate the pulse response of a system using persistent excitation signals (for example, wideband random inputs), this approach may not be desirable in MEMS resonator applications. First, coupling between the excitation and pick-off electrodes can easily obscure the resonator's motional response, eg. [14], and the use of persistent signals will always include effects of coupling due to the signal processing that is used to derive the pulse response estimate. Second, the smoothing required to recover the pulse response from input-output data generated with persistent input signals is generally associated with long testing times in order to obtain accurate estimates of mean-square spectra or correlation functions. It is important that the resonator dynamics be time invariant during such tests, however, this may be difficult to achieve in some cases, eg. modal frequency drift due to small changes in resonator temperature.

The proposed testing technique employs a periodic burst chirp signal applied to each input channel. The burst energy is constrained to be in a neighborhood of a pair of degenerate modes and, thus, produces a strong response from these modes. One period of the scalar-valued periodic burst chirp excitation signal v, written as a continuous-time function, is

$$v(t) = \begin{cases} 0, & t \in [0, \tau_p - \tau_b) \\ a\cos\big(2\pi f_{\text{ch}}(t)(t - \tau_p + \tau_b)\big), & t \in [\tau_p - \tau_b, \tau_p) \end{cases} \tag{6}$$

The time-dependent frequency of the burst is given by

$$f_{\text{ch}}(t) = \frac{1}{2\tau_b}(f_{\text{hi}} - f_{\text{low}})(t - \tau_p + \tau_b) + f_{\text{low}}. \tag{7}$$

The duration of the burst is τ_b seconds, τ_p is the signal period ($\tau_p > \tau_b$), and a is the amplitude of the burst. This signal concentrates its energy in the frequency band $[f_{\text{low}}, f_{\text{hi}}]$ Hz. The burst duration, amplitude and the frequency band where its energy is concentrated are easily adjusted using parameters in the time-domain description of the function. The phase of burst is chosen so that the burst occurs at the *end* of the period. Both input channels are stimulated with the periodic burst chirp (6), however, a time delay equivalent to half a period is introduced between the bursts appearing in each channel, in other words, the resonator input is defined

$$\vec{u}(t) = \begin{bmatrix} v(t) \\ v(t - \tau_p/2) \end{bmatrix} \tag{8}$$

where $\tau_p/2 > \tau_b$ so that there is an input-free transient period between bursts. Discrete-time versions of these signals are defined as $v_k = v(kt_s)$ and $\vec{u}_k = \vec{u}(kt_s)$,

$$v_k = 0, \quad k \in [0, N_p - N_b - 1]$$

and

$$\begin{aligned} v_k = & a\cos\big(2\pi f_{\text{ch},k}(k - N_p + N_b)t_s\big) \\ & k \in [N_p - N_b, N_p - 1], \end{aligned}$$

where $f_{\text{ch},k} = f_{\text{ch}}(kt_s)$ is an appropriate update of the frequency function in (7). The signal processing equipment implements the discrete-time signals such that there are N_p samples in one period and N_b samples in the burst portion of the signal ($N_p t_s = \tau_p$ and $N_b t_s = \tau_b$). It is also assumed that the number of points in one period is even (this simplifies notation in the analysis to follow and can be relaxed). The signal (8) is implemented as the input for all tests reported in this paper. The period and chirp frequency range are adjusted to suit the testing of a specific pair of modes. An example of $\vec{u}$ is shown in Fig. 4 where $\tau_b = 1$ second and $\tau_p = 10$ seconds. The chirp frequency range is chosen to excite either the $n = 1$, $n = 2$ or $n = 3$ pair of modes, however, the sinusoidal oscillation of the chirp cannot be resolved on the displayed time scale. It is necessary to stagger the bursts as shown in (8) because simultaneously applying the same stimulus to each input channel is equivalent to exciting the resonator with a single "virtual" electrode –such a test may not adequately excite both modes in a degenerate pair (for example, the virtual electrode may be located near a radial node of the mode shape and therefore will weakly couple to that mode).

C. Defining the Hankel matrices

The transient data between bursts is used to form the block-Hankel matrices (2). Since $\vec{u} = 0$ in these intervals, there is no parasitic input-output coupling and so the resonator model built from this data will not feature this coupling. An example of measurements when the bursts are designed to excite the $n = 1$ pair are shown in Fig. 5. The data segment corresponding to $t \in [0, 3]$ (highlighted red) is used in lieu of the first column of the resonator's pulse response, and the data segment corresponding to $t \in [5, 8]$ (also highlighted red) is substituted for the second column of the resonator's pulse response. Since $t_s = 1/70000$ second, there are over 200k data points recorded from each each pick-off for each transient data segment. The data used for modeling the resonator is acquired in a time interval that is less than one period of the input and in essence provides a "snapshot" of the resonator dynamics that is less susceptible to temperature-induced drift.

In contrast to the traditional Ho-Kalman procedure, this analysis does not directly yield the state-space B matrix but instead identifies "initial conditions" for the model's state vector at the start of the two data segments (at $t = 0$ and $t = 5$ in Fig. 5). Let $\vec{x}_{0,1}, \vec{x}_{0,2} \in \mathbb{R}^{n_s}$ correspond to the model state at $t = 0$ and $t = 5$, respectively. Define $X = \begin{bmatrix}\vec{x}_{0,1} & \vec{x}_{0,2}\end{bmatrix}$. The transient responses are assumed to be generated by $Y_k = CA^kX \in \mathbb{R}^{8\times 2}$, $k \geq 0$, where the index value $k = 0$ refers to the first data sample in both data segments. The Hankel matrices for this scenario are slightly modified with a shift in indices,

$$\mathcal{H}_0 = \begin{bmatrix} Y_0 & Y_1 & \cdots \\ Y_1 & Y_2 & \cdots \\ \vdots & \vdots & \ddots \end{bmatrix}, \quad \mathcal{H}_1 = \begin{bmatrix} Y_1 & Y_2 & \cdots \\ Y_2 & Y_3 & \cdots \\ \vdots & \vdots & \ddots \end{bmatrix}. \tag{9}$$

Note that

$$\mathcal{H}_0 = \mathcal{O}\mathcal{C}_X, \quad \mathcal{H}_1 = \mathcal{O}A\mathcal{C}_X, \tag{10}$$

where $\mathcal{O}$ is given in (4) and $\mathcal{C}_X$

$$\mathcal{C}_X = \begin{bmatrix} X & AX & A^2X & \cdots & A^{n_c-1}X \end{bmatrix} \in \mathbb{R}^{n_s \times n_i n_c}.$$

Thus, analysis of $\mathcal{H}_0$ and $\mathcal{H}_1$ yield A, C and X for the pair of modes under consideration.

The number of block-columns and block-rows in the Hankel matrices are denoted n_c and n_r. In general, one dimension must be large enough to accurately capture the time constants of the modes. A lower bound for the number of transient data points required in the analysis can be estimated. Suppose a resonant mode has modal frequency f Hz and time constant τ seconds. For standard sampling of the resonator transient response at least four samples per period of oscillation is desirable so $f_s > 4f$, where f_s is the sampling rate in Hz ($f_s = 1/t_s$, for sample period t_s seconds). An accurate measurement of the resonator time constant requires a data record of minimum length, for example, τ seconds (one time constant). Thus, the number of points in the transient data record that is used to form the Hankel matrices must be at least $f_s\tau > 4f\tau \approx Q$, where Q is the quality factor associated with the mode. For high quality factor resonators, the data sets can become quite large and although storage is typically not an issue, the analysis of large Hankel matrices can require significant computation. The "zoom" technique proposed in Sec. VI significantly reduces the burden of storing and processing large data sets.

D. Modal frequencies, damping, and orientation

The A and C matrices can be analyzed for modal frequencies, damping and mode orientation. Since the identified model is obtained by sampling a continuous-time system with sample period t_s, a mode with exponential decay rate σ (units of s^{-1}) and modal frequency ω_n (units of rad/s) will be associated with eigenvalues of the form $e^{(-\sigma \pm j\omega_n)t_s}$, where $j = \sqrt{-1}$. Thus, analysis of the eigenvalues of A yield the modal frequencies and time constants.

The mode orientation can be determined from the eigenvectors of A. First, referring to the pick-off electrode arrangement in Fig. 2, the angular reference bisects the S_1 pick-off electrode and establishes the origin for angle measurements and hence the orientation of a mode shape. The position of S_1 with respect to the angle origin is denoted $\theta_1 = 0°$, the position of S_2 with respect to the angle origin is denoted $\theta_2 = 15°$ and so forth through S_8 with $\theta_8 = 315°$. Although the mode shapes for the resonator in Fig. 2 do contain higher-order harmonics in θ, eg. [5], they are very small in amplitude compared to the dominant terms. Thus, it is assumed a mode shape is defined by $a\cos(2n(\theta - \phi))$, where ϕ is the orientation, for a mode in the n^{th} pair of degenerate modes. The amplitude of the mode shape as measured by the pick-off electrodes is proportional to

$$\begin{bmatrix} a\cos(2n(\theta_1 - \phi)) \\ a\cos(2n(\theta_2 - \phi)) \\ \vdots \\ a\cos(2n(\theta_8 - \phi)) \end{bmatrix} = \underbrace{\begin{bmatrix} \cos(2n\theta_1) & \sin(2n\theta_1) \\ \cos(2n\theta_2) & \sin(2n\theta_2) \\ \vdots & \\ \cos(2n\theta_8) & \sin(2n\theta_8) \end{bmatrix}}_{\Theta} \begin{bmatrix} \alpha \\ \beta \end{bmatrix}$$

where $\alpha = a\cos(2n\phi)$ and $\beta = a\sin(2n\phi)$, and Θ is defined as indicated. The objective is to determine α and β from analysis of the identified model. Let $\vec{w}$ be an eigenvector of A corresponding to eigenvalue $e^{(-\sigma+j\omega_n)t_s}$ and consider the unforced response of the resonator with initial condition $\vec{x}_0 = \frac{1}{2}(\vec{w} + \vec{w}^*)$, where * denotes complex-conjugate. This initial condition only involves one mode. The transient response, as measured by the pick-offs, would be

$$\begin{aligned} y_k &= CA^k \frac{1}{2}(\vec{w} + \vec{w}^*) \\ &= e^{-\sigma k t_s}\cos(\omega_n k t_s)\mathrm{Re}(C\vec{w}), \end{aligned}$$

where $\mathrm{Re}(C\vec{w}) \in \mathbb{R}^8$ denotes the real part of $C\vec{w}$. Alternatively, the imaginary part of $C\vec{w}$ can be used since this corresponds to replacing cos with sin in the transient response. Assuming the anti-alias filters are identical, an element of $\mathrm{Re}(C\vec{w})$ represents the amplitude of the mode shape expressed at the electrode of the corresponding measurement channel. Thus, α and β are determined from the following least squares problem,

$$\arg\min_{\alpha,\beta} \left\| \Theta \begin{bmatrix} \alpha \\ \beta \end{bmatrix} - \mathrm{Re}(C\vec{w}) \right\|,$$

TABLE I: Burst chirp input parameters

Pair	f_{low} (Hz)	f_{hi} (Hz)	a (V)	τ_p (s)	τ_b (s)
$n=1$	6525	6625	9	10	1
$n=2$	13500	13600	9	10	1
$n=3$	23825	23925	9	10	1

TABLE II: Five largest singular values of $\mathcal{H}_0$

Pair	σ_1	σ_2	σ_3	σ_4	σ_5	σ_4/σ_5
$n=1$	338	315	226	212	0.12	1841
$n=2$	154	147	124	118	0.09	1332
$n=3$	15.9	12.6	12.1	9.6	0.12	81

where $\|\cdot\|$ denotes the Euclidean norm. The orientation ϕ of the mode with respect to the angle reference is computed from α and β.

E. Complete resonator model

The B matrix in the resonator model can be determined once A and X have been extracted from the Hankel matrix analysis. The relationship between the columns of B, denoted $\vec{b}_1, \vec{b}_2 \in \mathbb{R}^{n_s}$, and X is

$$\begin{bmatrix}\vec{x}_{0,1}\\ \vec{x}_{0,2}\end{bmatrix} = \begin{bmatrix} I & A^{N_p/2}\\ A^{N_p/2} & I\end{bmatrix}\begin{bmatrix}\Gamma\vec{b}_1\\ \Gamma\vec{b}_2\end{bmatrix}, \tag{11}$$

where

$$\Gamma = (I - A^{N_p})^{-1}\left(\sum_{k=0}^{N_p-1} A^{N_p-1-k} v_k\right) \in \mathbb{R}^{n_s\times n_s}.$$

The resonator is asymptotically stable due to the fact that there is always some energy dissipation so $\det\left(I - A^{N_p}\right) \neq 0$. Therefore, Γ is always well-defined. The determinant of the matrix in (11) is equal to $\det\left(I - A^{N_p-2N_b}\right)$ and is similarly non-zero. Although the details are not provided here, (11) is easily established by simulating the model from the identified initial conditions and knowledge of the burst chirp signal, v_k. This analysis assumes the resonator has settled into its periodic response to the periodic input $\vec{u}$.

IV. Identification Results

The modeling results for the $n = 1, 2, 3$ pairs of modes are presented in this section. The period of the input is 10 seconds in all cases, however, the burst chirp frequency parameters are tailored to a given pair based on the modal frequencies estimated from Fig. 3. The input signal parameters are reported in Table I. The chirp frequency span is 100 Hz. The burst amplitude is 9 volts and its duration is 1 second ($t_s = 1/70000$ second, $N_p = 700\,\text{k}$ and $N_b = 70\,\text{k}$). The block-Hankel matrices have the same dimension $n_r = 5$ for all cases, however, $n_c = 210000$ for $n = 1, 2$, and $n_c = 105000$ for $n = 3$. These choices correspond to using 3 seconds and 1.5 seconds of transient data in the formation of $\mathcal{H}_0$ and $\mathcal{H}_1$ –this is adequate to accurately identify the time constants associated with the modes.

The five largest singular values of $\mathcal{H}_0$ for each case ($V_{\text{bias}} = 0$) are given in Table II. Since σ_4 exceeds σ_5 by at least two orders of magnitude in all cases, $\mathcal{H}_0$ is approximated by a rank 4 matrix. Thus, $n_s = 4$ and A, C and X are obtained from analysis of $\mathcal{H}_{0,4}$ and $\mathcal{H}_1$. The quality of the models can be assessed by simulating the model from the identified initial conditions: $CA^k\vec{x}_{0,1}$, $k \geq 0$, is compared to the transient response measurements starting at $t = 0$; similarly $CA^k\vec{x}_{0,2}$, $k \geq 0$, is compared to the transient response measurements starting at $t = 5$. Residuals are formed from the difference between the simulations and measurements (over the same 3 second data segment used in forming the Hankel matrices), thus, there is a residual associated with $\vec{x}_{0,1}$ and with $\vec{x}_{0,2}$. Since each residual has eight "channels" corresponding to the eight pick-offs, the power spectrum of each channel is computed and then summed to scalar-valued functions of frequency –the square roots are graphed and compared the measured baseline noise spectrum. The baseline noise spectrum is same for all tests. In a similar manner, the power in the transient signals are computed for the time intervals starting at $t = 0$ and $t = 5$ (although the transient response of the resonator is not a stationary signal the PSD computation still quantifies its power distributed as a function of frequency over the 3-second interval). In order to have a reasonable degree of smoothing for the relatively short duration data sets, the frequency resolution is only 100 Hz. The power in transient should be much larger than the power in the residual in a neighborhood of the pair of modes under test if the model is accurately reproducing the transient response.

The frequency response of the models is also compared to non-parametric frequency response estimates. The columns of the model's B matrix are determined according to Sec. III-E and then the discrete-time frequency response is computed via $C\left(e^{j\omega t_s} - A\right)^{-1} B$, where ω is the frequency variable in units of rad/s and $B = \begin{bmatrix}\vec{b}_1 & \vec{b}_2\end{bmatrix}$. The non-parametric frequency response is estimated from single-input-at-a-time tests using a periodic band-limited chirp excitation signal. The ratio of the discrete Fourier transform (DFT) of one period of a pick-off measurement to the DFT of one period of the input (applied to either D_1 or D_2) yields the empirical frequency response estimate for the corresponding input-output channel. The non-parametric method includes the effects of input-to-pick-off, or "feedthrough", coupling. The parametric models, however, completely reject any feedthrough and only show components associated with resonator motion.

The feedthrough is largely associated with capacitive coupling between electrodes, and since the input electrodes are driven by buffered voltage sources, the currents picked up by the pick-off electrodes generally increase with increasing frequency. This creates the trend in Fig. 3 up to the bandwidth of the pick-off buffers which is approximately 30 kHz. The feedthrough can be estimated using the models and measurement data: 1) the model is simulated over the time window that the burst is active; 2) this result is subtracted from the contemporaneous measurement data to produce a short (about τ_b second) record of data that has had the resonator motional component removed; 3) the non-parametric frequency response estimate is applied to this short segment along with the corresponding segment of burst chirp signal.

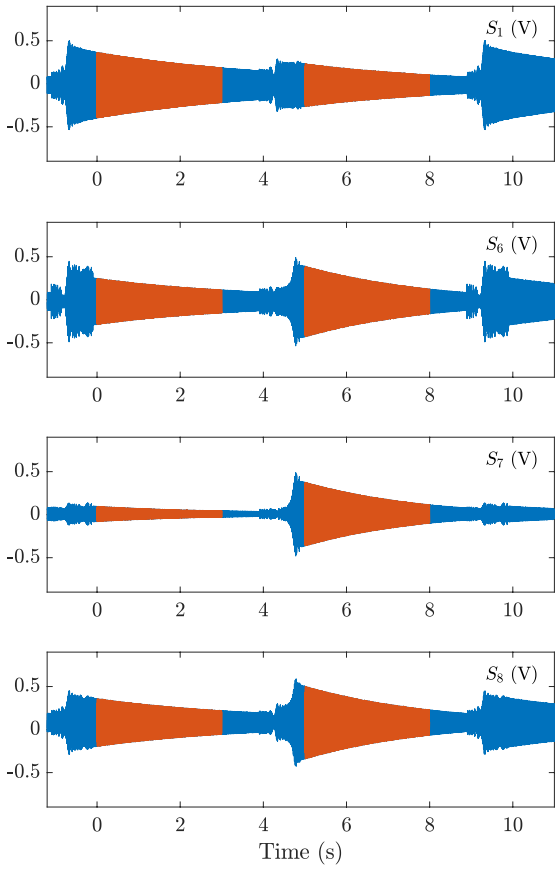

Fig. 5: Response of $n = 1$ modes to the input in Fig. 4. Only a subset of the pick-offs are shown (four, out of eight, pick-offs). The data highlighted in red is used to form the Hankel matrices after detrending to remove offsets. The model state $x_{0,1}$ is associated with $t = 0$, while $x_{0,2}$ is associated with $t = 5$.

TABLE III: $n = 1$ modal properties extracted from model

f_1 (Hz)	f_2 (Hz)	τ_1 (s)	τ_2 (s)	ϕ_1 (deg)	ϕ_2 (deg)
6559.17	6604.80	4.66	2.45	7.3	-82.3

Although the short data records do not give high frequency resolution, this is typically not necessary since the feedthrough is nearly constant in a small neighborhood of the modes. The feedthrough is significant for the $n = 2, 3$ modes and so it is estimated for these cases.

A. *Results for the $n = 1$ modes*

The periodic response of the resonator is shown in Fig. 5 for a subset of pick-offs. The power spectra of the transient, the residual and pick-off noise are shown in Fig. 6. An interesting feature in the spectra in Fig. 6 is the presence of the second harmonic near 13 kHz. This harmonic is not captured by the linear resonator model and so the power in the residual and transient data PSDs are equal in a neighborhood of this harmonic. The modal properties extracted from the identified model are given in Table III and the frequency response of the model and a non-parametric estimate are compared in Fig. 7.

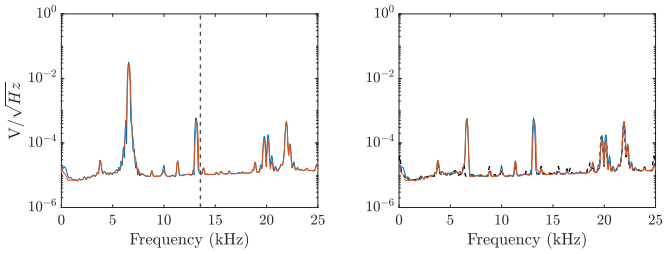

Fig. 6: (Left) Spectra associated with the transient data used for model development (the two traces correspond to the transients starting at $t = 0$ and $t = 5$). The $n = 1$ modes are near 6.6 kHz. A second harmonic is also evident. The dashed vertical line is located at the $n = 2$ modal frequencies. (Right) Spectra of the residuals (red, blue) compared to the noise floor (dashed, black). The model has removed significant power from the transient data at the $n = 1$ modal frequencies. The model is linear and does not capture the harmonic distortion near 13 kHz.

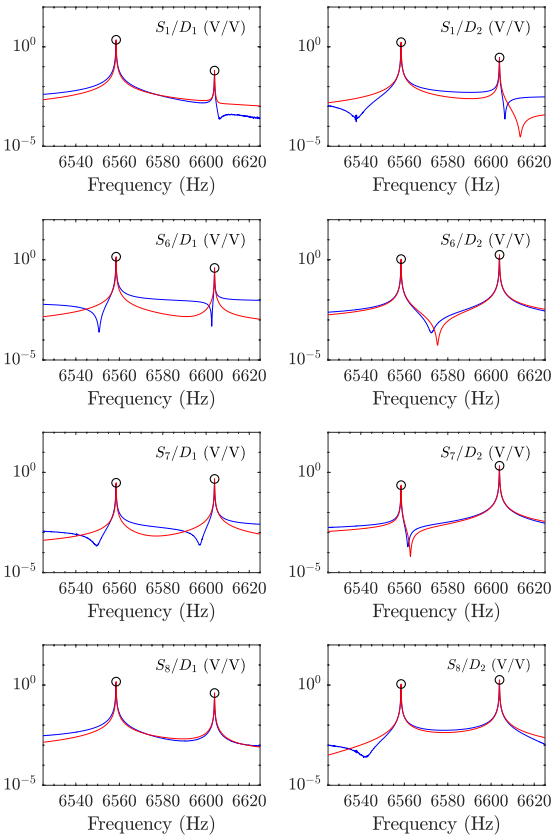

Fig. 7: Non-parametric frequency response magnitude (blue) is compared to the model frequency response (red) for the $n = 1$ pair of modes. The "○" are derived from analysis of the model's eigenvectors –see Sec. V.

B. *Results for the $n = 2$ modes*

The $n = 2$ pair of modes is an interesting case because this pair has been "tuned" using the algorithm introduced in [5] and deposition technique from [4]. The modal frequencies are very nearly equal and separate resonances cannot be distinguished in frequency response plots. Nevertheless, the modeling technique is able to clearly identify two modes and, importantly, their mode orientations. The periodic response of the resonator is shown in Fig. 8 for a subset of the pick-offs when $V_{\text{bias}} = 0$.

As a further demonstration of power of the proposed mod-

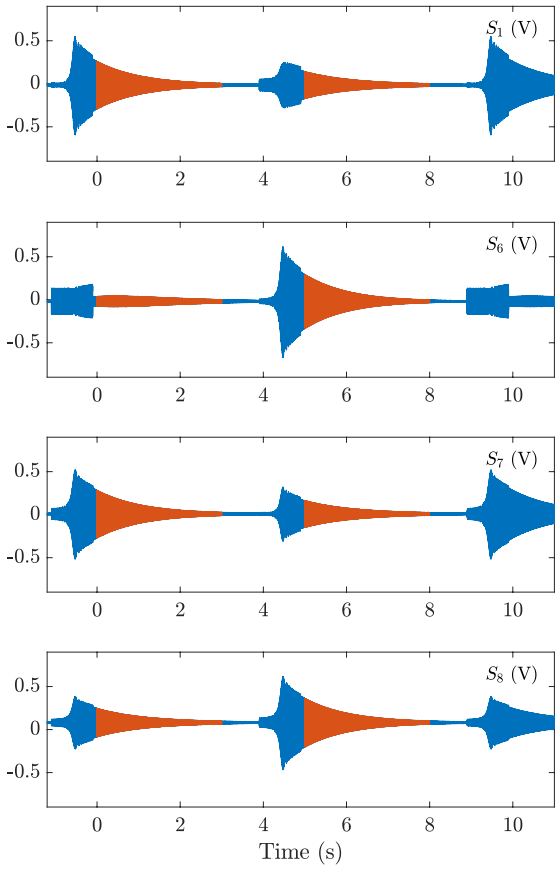

Fig. 8: Response of $n = 2$ modes to the input in Fig. 4 when $V_{\text{bias}} = 0$. Only a subset of the pick-offs are shown (four, out of eight, pick-offs). The data highlighted in red are used to form the Hankel matrices after detrending to remove offsets.

TABLE IV: $n = 2$ modal properties determined from model

	V_{bias} (V)			
	0	15	30	45
f_1 (Hz)	13548.95	13548.89	13548.87	13548.79
f_2 (Hz)	13549.04	13548.96	13548.90	13548.85
$f_2 - f_1$	0.09	0.07	0.03	0.06
τ_1 (s)	1.08	1.08	1.08	1.08
τ_2 (s)	1.08	1.08	1.08	1.08
ϕ_1 (deg)	-3.7	-2.3	5.5	31.0
ϕ_2 (deg)	41.4	42.8	50.5	75.8
$\lvert\phi_2 - \phi_1\rvert$	45.1	45.1	45.0	44.8

eling technique, the $n = 2$ modes are perturbed by applying $V_{\text{bias}} \neq 0$. The perturbed modes exhibit small changes in modal frequencies, however, it is shown that the mode orientations are quite sensitive to V_{bias}. A summary of the modal properties are given in Table IV. Fig. 9 compares the PSD of the residual to the PSD of the transient data when $V_{\text{bias}} = 0$. The frequency response of the model versus a non-parametric estimate is shown in Fig. 10. Significant feedthrough is evident in certain input-output channels.

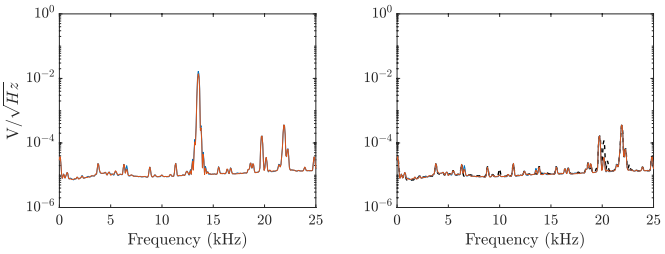

Fig. 9: (Left) Spectra associated with the transient data used for model development (the two traces correspond to the transients starting at $t = 0$ and $t = 5$). The modes are near 13.5 kHz. (Right) Spectra of the residuals compared to the noise floor (dashed, black). The residual spectra are essentially equal to the noise spectrum.

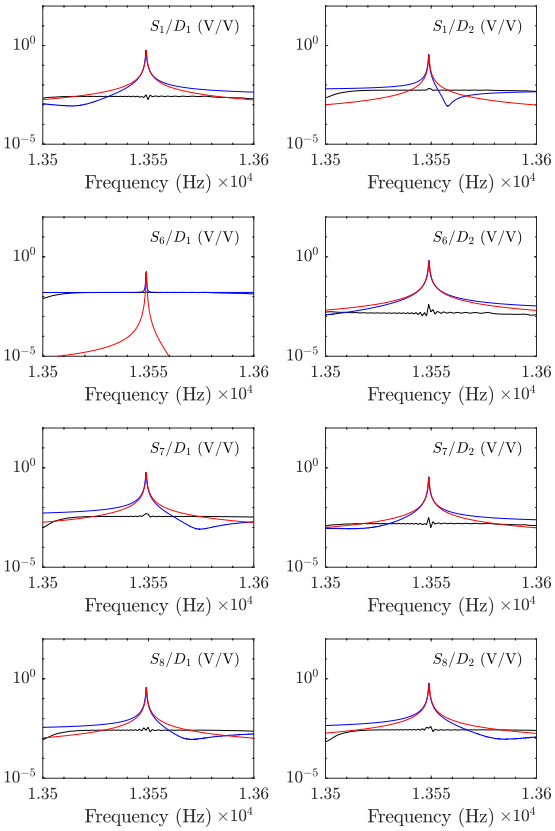

Fig. 10: Frequency response magnitudes showing the $n = 2$ pair of modes. The non-parametric estimate (blue) has significant feedthrough coupling (black line) in some input-output channels. The model frequency response (red) is not afflicted by the coupling.

C. *Results for the $n = 3$ modes*

The response of the resonator to the periodic burst chirp input adapted to excite the $n = 3$ pair of modes is shown in Fig. 11. The feedthrough coupling is quite evident in the time response. The five largest singular values of $\mathcal{H}_0$ are reported in Table II. A summary of the modal frequencies and mode orientations extracted from the 4-state model are given in Table V. The power spectrum of the residual and transient are shown in Fig. 12. Finally, Fig. 13 compares the frequency responses of the model and non-parametric estimate.

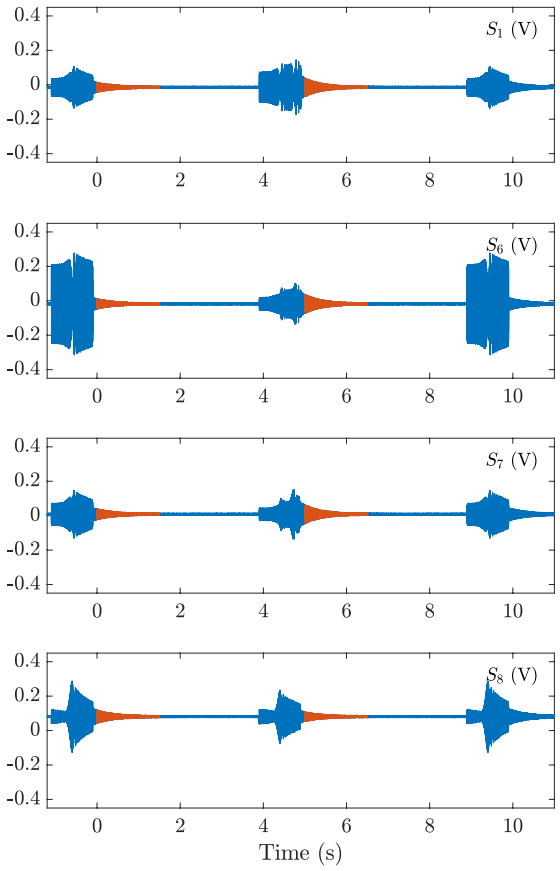

Fig. 11: Response of $n = 3$ modes to the input in Fig. 4 when $V_{\text{bias}} = 0$. Only a subset of the pick-offs are shown (four, out of eight, pick-offs). The data highlighted in red is used to form the Hankel matrices. The feedthrough coupling is a significant issue for these modes as evidenced by the measurement values at the times the burst is active, cf. Fig. 4.

TABLE V: $n = 3$ modal properties determined from model

f_1 (Hz)	f_2 (Hz)	τ_1 (s)	τ_2 (s)	ϕ_1 (deg)	ϕ_2 (deg)
23867.31	23901.07	0.43	0.43	15.5	-14.5

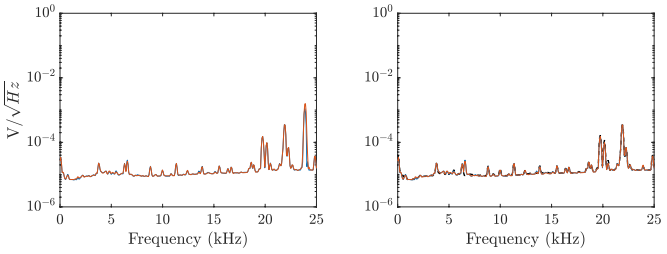

Fig. 12: (Left) Spectra associated with the transient data used for model development (the two traces correspond to the transients starting at $t = 0$ and $t = 5$). The modes are near 24 kHz. (Right) Spectra of the residuals compared to the noise floor (dashed, black).

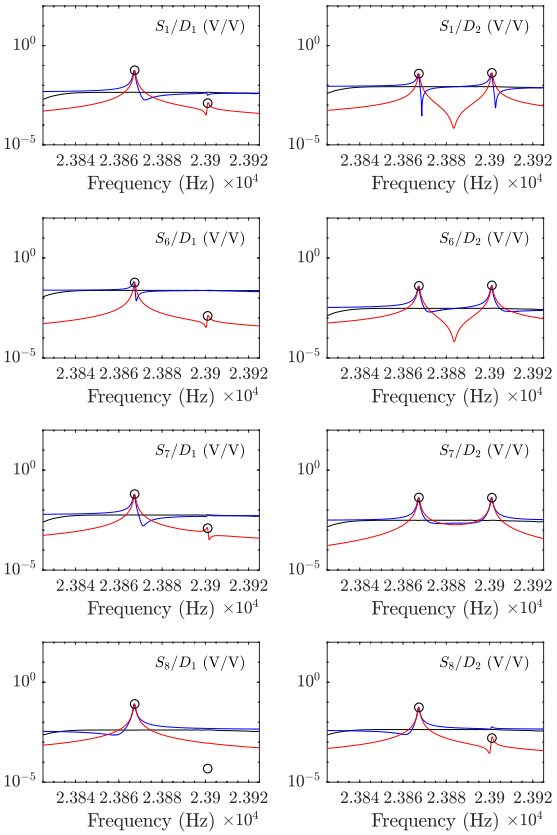

Fig. 13: Non-parametric (blue) and model (red) frequency response magnitude for the $n = 3$ modes. The estimated feedthrough coupling is also shown (black). The "○" are derived from analysis of the model's eigenvectors –see Sec. V.

V. Discussion

The veracity of the identified models is confirmed in several ways. First, comparing model and non-parametric frequency responses shows very close agreement between the resonant frequencies and peak magnitude at these frequencies. The model and non-parametric frequency responses differ away from the resonant frequencies, though, because of the feedthrough coupling. Although not shown here, if the feedthrough estimate is summed with the model frequency response, the non-parametric frequency response is recovered.

The mode orientations can also be estimated from the magnitudes of the frequency responses at a given resonant frequency –mapping the magnitudes to the electrode locations gives insight into orientation of the mode under consideration. This approach can only be applied when the modal frequencies are significantly detuned because the two modes respond in an essentially decoupled manner. The model yields mode orientations that are consistent with the non-parametric frequency responses in the $n = 1, 3$ cases. For these cases the elements of $\text{Re}(C\vec{w})$ are graphed in the frequency response plots at the modal frequency corresponding to the eigenvector $\vec{w}$. Since all elements can be scaled by the same factor without changing the mode shape, the scaling is employed to match one element in $\text{Re}(C\vec{w})$ to the frequency response magnitude. Figs. 7 and 13 show the scaled elements of $\text{Re}(C\vec{w})$ for both modes as the "○" points –note how all of these amplitude

estimates using the eigenvector coincide with the frequency response magnitudes at the resonant frequencies. This confirms that mode orientations derived from the models are consistent with those derived from the frequency response plots.

The spectra of the residuals compared to the noise floor and spectra of the transient data is a measure of how well the model captures the transient response measurements. The residual in the $n = 2, 3$ cases is indistinguishable from the noise floor measurement. In other words, the model has removed any trace of the transient response from the residual. The $n = 1$ residual still shows some power at the modal frequencies but the RMS value of the residual is more than two orders of magnitude smaller than the transient response RMS value. Also note that the model identifies poorly matched time constants for these modes. The time constant mismatch is not readily apparent from the time domain data because both modes are mixed into each output channel. Although the source of the mismatched time constants has not been identified with certainty, the fact that the $n = 1$ modes are not isolated from the substrate makes them very susceptible to the boundary conditions/mounting method of the die (in contrast, the $n = 2, 3$ pairs are nominally isolated from the substrate). It was mentioned in Sec. III-A that the resonator die is suspended from wire bonds. This mounting method reduces interaction between the die and its supporting substrate when testing the $n = 1$ modes. Although this mounting method produces the longest time constants for the $n = 1$ modes, the time constants are still sensitive to how the wire bonds are attached to the buffer board, e.g., removing and reattaching the die will change the $n = 1$ time constants. The sensitivity of the $n = 1$ modes to its boundary conditions, and the fact that they are very susceptible to vibration imposed on the die, make them unsuitable for exploitation in vibratory gyros, however, they are included here to demonstrate the generality of the proposed modeling method.

Finally, the mode orientations obtained from the models should conform to known properties of modally degenerate ring-type resonators. The mode orientations determined from analysis of the models satisfy $|\phi_1 - \phi_2| \approx 90°/n$ with at most a $0.5°$ deviation for all of the cases considered in Sec. IV, including the $n = 2$ modes for different values of V_{bias}. This result is consistent with the modal properties of slightly perturbed ring resonators. It is important to note that the model was in no way constrained to enforce a relationship between the orientations of the modes in a given pair –this observation lends considerable credibility to the modeling approach. Further investigation of the $n = 2$ modes yields additional insight. The modal frequencies are weakly perturbed by V_{bias} as shown in Table IV yet the mode orientations are very sensitive to V_{bias}. This behavior is well-known in structural systems with nearly equal eigenvalues: although the eigenvalues are continuous functions of the perturbation parameter (in this case the "stiffness" created by the electrostatic force gradient when $V_{\text{bias}} \neq 0$), the eigenvectors are generally not continuous functions of the perturbation parameter so it is no surprise that the mode orientations display sensitivity to V_{bias}.

The foregoing discussion addresses the ability of the model to provide accurate modal information for degenerate mode resonators. One outstanding issue is why the first four singular values of $\mathcal{H}_0$ are orders of magnitude larger than the remaining singular values. This fact implies that a model order of four ($n_s = 4$) can accurately represent the transient data. The anticipated *minimum* model order is four because this corresponds to the two oscillator model that is necessary to capture both modes in a degenerate pair, however, the testing block diagram in Fig. 1 shows that the smoothing and anti-alias filters filters are part of the signal chain that includes the resonator and, thus, their effects are present in the measurements. There are a total of 76 states associated with these filters –each of the eight pick-offs is filtered by an 8-pole anti-alias filter and each of the two resonator inputs is preceded by a 6-pole smoothing filter. Despite the large number of states in these filters, the analysis in Sec. IV shows that a 4-state model can very accurately reproduce the transient measurement data. Although this appears contradictory, the truncation of $\mathcal{H}_0$ to a rank 4 matrix preserves the dynamic features that produce the highest energy in the pick-off measurements. These high energy modes are actually the resonator's modes due to their relatively long time constants when compared to the time constants of the anti-alias and smoothing filters. Nevertheless, the filters do contribute gain and phase shifts to the measurement data and, therefore, must be reflected in some manner in the 4-state models.

Presenting the details of this analysis would deviate too far from the main point of the paper, however, a brief explanation is provided. It was shown in [24] that as modal damping goes to zero, balanced coordinates coincide with modal coordinates in a state-space representation of a system. Since the Hankel matrix modeling technique produces models that are equivalent to models based on balanced truncation (using finite-time gramians), a realization of the system that includes the four resonator states and the filter dynamics can be transformed into block modal form. Truncating all of the states except the resonator states yields an "A" matrix whose eigenvalues match those of the resonator, however, the magnitude and phase shifts produced by the smoothing and anti-alias filters in a neighborhood of the resonator modal frequencies are embedded into the B and C matrices of the truncated realization. Thus, the Hankel matrix analysis produces a model in which the resonator modes are faithfully captured, however, the identified B and C matrices include the effects of the input and output filters.

VI. Zoom Analysis

The Hankel matrices analyzed in Sec. IV have dimension up to 40×420000 ($n_r = 5$, $n_o = 8$, $n_c = 120000$ and $n_i = 2$). The column dimension must be large in order to faithfully capture the modal time constants. Although an "economy" SVD can efficiently produce the necessary factorization for modeling, it is possible to greatly reduce both the size of the test data sets and dimension of the Hankel matrices without compromising the integrity of the models. The proposed approach is termed "zoom analysis" given its similarity to the signal processing used in "zoom-FFT" spectral analysis [25].

Since the transient response of a pair of degenerate modes is a narrow-band phenomenon, it is possible to downsample the

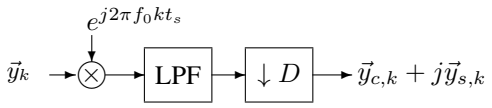

Fig. 14: Block diagram for zoom analysis. The demodulated signals $\vec{y}_{c,k}$ and $\vec{y}_{s,k}$ are used to form the Hankel matrices, however, the decimation operation greatly reduces the size of the data sets and, thus, the dimensions of the Hankel matrices.

response using demodulation frequency f_0 in a neighborhood of the pair of modes under study. Fig. 14 illustrates how the sampled resonator output $\vec{y}_k$ is manipulated –it is the same block diagram that is used for standard zoom spectral analysis, however, the downsampled data sequences, denoted $\vec{y}_{c,k}$ and $\vec{y}_{s,k}$ are now used to form $\mathcal{H}_0$ and $\mathcal{H}_1$. The sample period associated with $\vec{y}_{c,k}$ and $\vec{y}_{s,k}$ is $t_D = Dt_s$, where the positive integer D is the decimation factor, and "LPF" denotes unity DC gain low-pass filters that remove the high frequency products. The lower data rate associated with the demodulated signals is where the savings is realized. Since $\vec{y}_k$ is a vector-valued signal, the operations in Fig. 14 are performed element-wise. Note that the storage requirements are reduced by a factor of $D/2$ because the number of output channels is effectively doubled.

Non-parametric zoom-FFT techniques use the spectrum of the demodulated signals to recover the spectrum of the original signals in a neighborhood of ω_0. In the Hankel matrix analysis, though, it is necessary to convert the properties of the identified "baseband" model into properties of the resonator. In view of the modeling results in Sec. IV it can be assumed that the model generating the transient data is composed of m oscillators and is given by $\vec{y}_k = CA^k\vec{x}_0$, $k \geq 0$, where $A \in \mathbb{R}^{2m\times 2m}$, so $n_s = 2m$ ($m = 2$ for the resonator analyzed in this paper). The analysis proceeds by representing A in a special basis. Since the system is composed of m oscillators, the eigenvalues of A are given by $e^{(-\sigma_l \pm j\omega_l)t_s}$, $\omega_l > 0$, $l = 1, 2, \ldots, m$, where the exponential decay rate and modal frequency for the l^{th} mode are given by σ_l and ω_l, respectively. Even if there are some repeated eigenvalues, it is assumed that A is non-defective and so A is diagonalizable. Let the columns of $T^+ \in \mathbb{C}^{n_s\times m}$ span the A-invariant subspace associated with the eigenvalues $e^{(-\sigma_l+j\omega_l)t_s}$, $l = 1, 2, \ldots, m$. The complex-conjugate of T^+ is denoted T^-. The columns of T^- span the A-invariant subspace associated with the eigenvalues $e^{(-\sigma_l-j\omega_l)t_s}$. Since these invariant subspaces only intersect at 0, the matrix $T = \begin{bmatrix} T^+ & T^- \end{bmatrix} \in \mathbb{C}^{n_s\times n_s}$ is invertible. The change of basis yields a block diagonal format,

$$T^{-1}AT = \begin{bmatrix} A^+ & 0 \\ 0 & A^- \end{bmatrix}$$

where $A^+ \in \mathbb{C}^{m\times m}$ has eigenvalues $e^{(-\sigma_l+j\omega_l)t_s}$, $l = 1, 2, \ldots, m$, and A^- is the complex conjugate of A^+ with eigenvalues $\{e^{(-\sigma_l-j\omega_l)t_s}\}$. The measurement sequence from a transient response with initial condition $\vec{x}_0 \in \mathbb{R}^{n_s}$ is

$$\begin{aligned}\vec{y}_k &= CA^k\vec{x}_0 \\ &= CT\begin{bmatrix} (A^+)^k & 0 \\ 0 & (A^-)^k \end{bmatrix} T^{-1}\vec{x}_0.\end{aligned}$$

An expression for the demodulated components of $\vec{y}_k$ is derived. The demodulating sinusoid is assumed to be $\cos(\omega_0 kt_s)$, $\omega_0 = 2\pi f_0 > 0$. In general, the phase of the demodulating sinusoid should be an arbitrary parameter since it is not possible to control the phase relative to the data that is used for forming the Hankel matrices. Including a phase parameter only complicates the analysis without changing the fundamental result, thus, the phase is assumed to be zero as shown. Multiplying $\vec{y}_k$ by the sinusoid yields,

$$\begin{aligned}&\cos(\omega_0 kt_s)\vec{y}_k \\ &= \frac{1}{2}CT\begin{bmatrix} (A^+)^k e^{j\omega_0 kt_s} & 0 \\ 0 & (A^-)^k e^{j\omega_0 kt_s} \end{bmatrix} T^{-1}\vec{x}_0 \\ &\quad + \frac{1}{2}CT\begin{bmatrix} (A^+)^k e^{-j\omega_0 kt_s} & 0 \\ 0 & (A^-)^k e^{-j\omega_0 kt_s} \end{bmatrix} T^{-1}\vec{x}_0.\end{aligned} \tag{12}$$

The demodulation frequency ω_0 is selected to be near the set of frequencies $\{\omega_1, \omega_2, \ldots, \omega_m\}$. It is possible for ω_0 to be greater than these frequencies, less than these frequencies, or in the midst of this set. The examples shown below demonstrate that identified modal properties are robust to the choice of ω_0. The low-pass filter is designed so that its corner frequency is greater than $|\omega_l - \omega_0|$, $l = 1, 2, \ldots, m$, so that contributions from all oscillators are preserved in the demodulated signal. Furthermore, D is selected to avoid aliasing. This permits the truncation of the blocks in (12) that generate the terms with approximate frequencies $\pm 2\omega_0$ (the eigenvalues of $A^+e^{j\omega_0 t_s}$ and $A^-e^{-j\omega_0 t_s}$). The decimation operation simply replaces k with Dk in the right-hand side terms. The sample period of the downsampled data is $t_D = Dt_s$. Thus,

$$\vec{y}_{c,k} = \frac{1}{2}C\Phi^k\vec{x}_0, \tag{13}$$

where

$$\Phi := T\begin{bmatrix} (A^+)^D e^{-j\omega_0 t_D} & 0 \\ 0 & (A^-)^D e^{j\omega_0 t_D} \end{bmatrix} T^{-1} \in \mathbb{R}^{n_s\times n_s}.$$

It can be shown that Φ is real if A is real.

Application of the Hankel matrix analysis technique to the demodulated signal $\vec{y}_{c,k}$ will yield estimates for C, Φ and $\vec{x}_0$. Although C and $\vec{x}_0$ are associated with the original system, it is not possible to recover the modal frequencies ω_l, $l = 1, \ldots, m$, from analysis of Φ alone because the eigenvalues of Φ are the set $\{e^{(-\sigma_l \pm j(\omega_l-\omega_0))t_D}\}$ and it is not *a priori* known if the beat frequency $|\omega_l - \omega_0|$ corresponds to a mode whose natural frequency is greater than, or less than, the demodulation frequency ω_0. The ambiguity can be eliminated by considering the demodulated signal $\vec{y}_{s,k}$ in addition to $\vec{y}_{c,k}$.

The expression for $\vec{y}_{s,k}$ is

$$\begin{aligned}\vec{y}_{s,k} &= \frac{1}{2}CT\begin{bmatrix} j(A^+)^{Dk} e^{-j\omega_0 kt_D} & 0 \\ 0 & -j(A^-)^{Dk} e^{j\omega_0 kt_D} \end{bmatrix} T^{-1}\vec{x}_0 \\ &= \frac{1}{2}\underbrace{CM}_{C_s}\Phi^k\vec{x}_0,\end{aligned}$$

where

$$M = T\begin{bmatrix} jI & 0 \\ 0 & -jI \end{bmatrix} T^{-1} \in \mathbb{R}^{n_s\times n_s},$$

and the matrix $C_s \in \mathbb{R}^{n_0\times n_s}$ is defined as indicated. It is important to express $\vec{y}_{s,k}$ and $\vec{y}_{c,k}$ with the same dynamics

matrix Φ because the Hankel matrix analysis is applied to the base-band system with augmented outputs. The definition of Y_k is updated to

$$Y_k = \frac{1}{2}\begin{bmatrix} C \\ C_s \end{bmatrix} \Phi^k X, \quad k \geq 0$$

where X is the matrix of initial conditions associated with the transients starting at $t = 0$ and $t = 5$ as shown in Fig. 15. Analysis of the Hankel matrices formed from the demodulated data yield C, C_s, Φ and X.

The modal frequency and damping terms associated with the oscillators are determined as follows. Only a single output is necessary to describe the process so it can be assumed $\vec{y}$, and, hence, $\vec{y}_{c,k}$ and $\vec{y}_{s,k}$, are scalar-valued. Let $\vec{w} \in \mathbb{C}^{n_s}$ be an eigenvector of Φ whose corresponding eigenvalue is $e^{(-\sigma+j\tilde{\omega})t_D}$, where the eigenvalue is chosen so that $\tilde{\omega} > 0$. There are two cases to consider. Suppose the "baseband" frequency $\tilde{\omega}$ is associated with an oscillator whose frequency is greater than ω_0. In other words, $\tilde{\omega} = \omega_l - \omega_0$ for some $l \in [1, \ldots, m]$. In this case the eigenvector $\vec{w}$ may be expressed as $\vec{w} = T^+\vec{z}$ for some unique $\vec{z} \in \mathbb{C}^m$, $\vec{z} \neq 0$. The output matrix associated with the $\vec{y}_{c,k}$ "channel" is C and $C\vec{w} \in \mathbb{C}$ is its product with the eigenvector (since a single output is assumed for this argument). Without loss of generality, it is assumed $C\vec{w} \neq 0$ otherwise the pick-off associated with this output is located at a node of the mode and so no response is observed (another output channel must be selected). Represent $C\vec{w} = \alpha + j\beta$, $\alpha, \beta \in \mathbb{R}$. Now, consider the product of $\vec{w}$ with the output matrix associated with $\vec{y}_{s,k}$,

$$\begin{aligned} C_s\vec{w} &= CMT^+\vec{z} \\ &= jCT^+\vec{z} \\ &= -\beta + j\alpha \end{aligned}$$

Define the matrix $\mathcal{S} \in \mathbb{R}^{2\times 2}$

$$\mathcal{S} = \begin{bmatrix} \mathrm{Re}(C\vec{w}) & \mathrm{Im}(C\vec{w}) \\ \mathrm{Re}(C_s\vec{w}) & \mathrm{Im}(C_s\vec{w}) \end{bmatrix}. \tag{14}$$

For the case considered above, namely $\omega_l > \omega_0$,

$$\det \mathcal{S} = \det \begin{bmatrix} \alpha & \beta \\ -\beta & \alpha \end{bmatrix} = \alpha^2 + \beta^2 > 0$$

The second case to consider is when $\tilde{\omega} = \omega_0 - \omega_l > 0$, for some $l \in [1, \ldots, n]$. In this case, the demodulation frequency is greater than the oscillator frequency and the eigenvector $\vec{w}$ can be represented $\vec{w} = T^-\vec{z}$, for some unique $\vec{z} \in \mathbb{C}^m$, $\vec{z} \neq 0$. As before, suppose $C\vec{w} = \alpha + j\beta$ for a new set of $\{\alpha, \beta\}$. Consider,

$$\begin{aligned} C_s\vec{w} &= CMT^-\vec{z} \\ &= -jCT^-\vec{z} \\ &= \beta - j\alpha \end{aligned}$$

In this case, $\det \mathcal{S} = -(\alpha^2+\beta^2) < 0$. Thus, the sign of $\det \mathcal{S}$ determines whether the modal frequency is less than or greater than the demodulation frequency.

In summary, each output channel is demodulated to produce the baseband signals $\vec{y}_{c,k}$ and $\vec{y}_{s,k}$. A linear model is fit to the baseband data and yields C, C_s, Φ and x_0. Consider an eigenvalue/vector pair of Φ: $e^{(-\sigma+j\tilde{\omega})t_D}$ and $\vec{w}$, for which $\tilde{\omega} > 0$ (since the eigenvalues of Φ appear in conjugate-pairs, m eigenvalues can be chosen to satisfy this constraint). Selecting the same row in C and C_s, $\mathcal{S}$ is computed and the modal frequency of the oscillator is recovered from

$$\omega_0 + \tilde{\omega}\,\mathrm{sgn}\left(\det \mathcal{S}\right), \tag{15}$$

where sgn is the signum, or sign, function. This calculation can be performed for each output channel to check consistency of frequency estimates. The exponential decay rate σ is preserved in the demodulated data and so can be directly obtained from the eigenvalue $e^{(-\sigma+j\tilde{\omega})t_D}$.

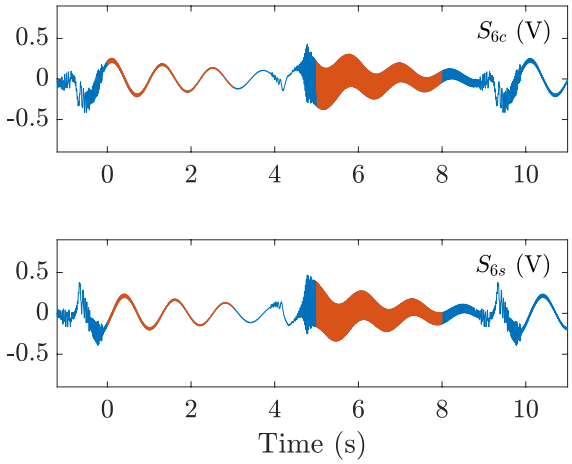

Fig. 15: An example of the S_6 electrode measurement of the $n = 1$ test from Fig. 5 demodulated with $f_0 = 6560$ Hz into components $\vec{y}_{c,k}$ (top) and $\vec{y}_{s,k}$ (bottom). The highlighted segments (red) are used to construct the Hankel matrices. The decimation factor is $D = 100$ so the sample period is $t_D = Dt_s = 1/700$ second.

A. *Zoom analysis applied to resonator*

The zoom technique is applied to the $n = 1, 2, 3$ resonator modes in order to determine modal frequencies, time constants, and mode orientations. In order to assess consistency with the results presented in Sec. IV, the same data sets are used for the zoom analysis since these data are stored and can be processed according to the zoom method. The low-pass filters are 4-pole Butterworth filters with 200 Hz corner frequencies and $D = 100$. The only parameter that is changed is ω_0 since that is dependent on the which pair of degenerate modes is to be analyzed (ω_0 is reported as f_0, with unit Hz, in the tables). As in the prior analysis, two 3-second transient data segments are used to form the Hankel matrices for $n = 1, 2$, so $n_r = 5$ and $n_c = 2100$, however, $n_o = 16$ because demodulation of $\vec{y}_k$ into $\vec{y}_{c,k}$ and $\vec{y}_{s,k}$ doubles the number of output channels. The dimensions of the Hankel matrices are now 80×4200. For $n = 3$, 1.5 seconds of data are used. An example of the demodulated S_6 pick-off for $n = 1$ is shown in Fig. 15 (compare to Fig. 5). The singular values of $\mathcal{H}_0$ are presented in Table VI for three demodulation frequencies applied to each pair of modes. Although the singular values are different from the non-zoom analysis, σ_4 remains more than two orders of magnitude larger than σ_5 so $n_s = 4$ is still a reasonable choice for the model order (demodulation reduces the signal power and this is reflected in the new

TABLE VI: Singular values of $\mathcal{H}_0$ for zoom analysis

Pair	f_0 (Hz)	σ_1	σ_2	σ_3	σ_4	σ_5	σ_4/σ_5
	6550	46.0	45.8	30.8	30.7	0.0093	3291
$n=1$	6580	46.0	45.8	30.9	30.6	0.0095	3233
	6610	45.9	45.9	30.9	30.6	0.0093	3280
	13540	21.4	21.1	17.2	17.0	0.0071	2381
$n=2$	13550	22.7	19.8	18.3	15.8	0.0072	2186
	13560	21.4	21.1	17.2	17.0	0.0072	2348
	23860	2.01	1.98	1.58	1.53	0.0079	193
$n=3$	23880	2.04	1.94	1.60	1.51	0.0079	191
	23910	2.03	1.96	1.56	1.55	0.0081	192

singular values). Analysis of the Hankel matrices yields Φ, C, C_s and X for each demodulation frequency. The mode orientations can be determined using the process described in Sec. III-D with the eigenvectors of Φ without modification. The modal properties determined from the zoom analyses yield the *same* values as quoted in Tables III, IV and V so no separate summaries for the zoom analyses are required. Note that the modal properties are independent of the choice of f_0.

VII. Conclusion

The proposed parametric modeling technique yields accurate frequency, damping, and mode orientation estimates for degenerate pairs of modes. Test results are reported for $n = 1, 2, 3$ pairs of modes in an axisymmetric MEMS ring resonator. The technique rejects parasitic coupling between the input and output electrodes because the dynamic model is developed from transient, input-free data. The proposed technique is complementary to the non-parametric frequency response estimation methods that are ubiquitous in MEMS resonator testing. Parametric models have some distinct advantages when the difference between modal frequencies is sufficiently small such that individual quality factors and even modal frequencies are difficult to discriminate from frequency response graphs or ring-down data. The proposed modeling technique also yields mode orientations in these challenging cases. The relative mode orientations extracted from the identified models are consistent with the known properties of modally degenerate structures like rings. The model-based orientation estimates also agree with the empirical frequency response graphs when the modes were sufficiently separated in frequency. A "zoom" variation of the modeling technique based on fitting models to demodulated data greatly reduces the storage and signal processing requirements compared to the standard algorithm. Analysis of the models derived with zoom technique yielded identical modal property estimates for the various pairs of modes in the test resonator.

References

[1] T. Charnley and R. Perrin, "Perturbation Studies with a Thin Circular Ring," *Acta Acustica*, vol. 28, no. 3, pp. 139–146, 1973.

[2] C. H. J. Fox, "A simple theory for the analysis and correction of frequency splitting in slightly imperfect rings," *J. Sound Vib.*, vol. 142, no. 2, pp. 227–243, 1990.

[3] A. K. Rourke, S. Mcwilliam, and C. H. Fox, "Multi-mode trimming of imperfect rings," *J. Sound Vib.*, 2001.

[4] D. Schwartz, D. Kim, P. Stupar, J. DeNatale, and R. T. M'Closkey, "Modal parameter tuning of an axisymmetric resonator via mass perturbation," *J. Microelectromech. Sys.*, vol. 24, no. 3, pp. 545–555, 2015.

[5] A. H. Behbahani, D. Kim, P. Stupar, J. Denatale, and R. T. M'Closkey, "Tailored etch profiles for wafer-level frequency tuning of axisymmetric resonators," *J. Microelectromech. Sys.*, vol. 26, no. 2, pp. 333–343, 2017.

[6] C. Sanathanan and J. Koerner, "Transfer function synthesis as a ratio of two complex polynomials," *IEEE Trans. Autom. Control*, vol. 8, no. 1, pp. 56–58, January 1963.

[7] J. L. Adcock, "Curve fitter for pole-zero analysis," *Hewlett-Packard Journal*, vol. 38, no. 1, pp. 33–36, 1987.

[8] J. E.-Y. Lee and A. A. Seshia, "Direct parameter extraction in feedthrough-embedded capacitive mems resonators," *Sens. Actuator A Phys.*, vol. 167, no. 2, pp. 237–244, 2011.

[9] A. Brenes, J. Juillard, F. V. Dos Santos, and A. Bonnoit, "Characterization of mems resonators via feedthrough de-embedding of pulsed-mode response," *Procedia Eng.*, vol. 87, pp. 823–826, 2014.

[10] A. S. Phani and A. Seshia, "Identification of anisoelasticity and nonproportional damping in mems gyroscopes," in *NSTI-Nanotech*, vol. 2, 2004, pp. 343–346.

[11] D. Kim and R. T. M'Closkey, "A systematic method for tuning the dynamics of electrostatically actuated vibratory gyros," *IEEE Trans. Control Syst. Technol.*, vol. 14, no. 1, pp. 69–81, January 2006.

[12] C. C. Painter and A. M. Shkel, "Active structural error suppression in mems vibratory rate integrating gyroscopes," *IEEE Sens. J.*, vol. 3, no. 5, pp. 595–606, 2003.

[13] O. Kuter-Arnebeck, A. Labuda, S. Joshi, K. Das, and S. Vengallatore, "Estimating damping in microresonators by measuring thermomechanical noise using laser doppler vibrometry," *J. Microelectromech. Sys.*, vol. 23, no. 3, pp. 592–599, 2014.

[14] H. H. Ge, A. H. Behbahani, J. S. Gibson, and R. T. M'Closkey, "Adaptive cancellation of parasitic coupling," *J. Microelectromech. Sys.*, vol. 27, no. 5, pp. 844–853, 2018.

[15] R. T. M'Closkey, S. Gibson, and J. Hui, "System Identification of a MEMS Gyroscope ," *J. Dyn. Syst. Meas. Control*, vol. 123, no. 2, pp. 201–210, 06 1999.

[16] P. Shao, V. Tavassoli, C.-S. Liu, L. Sorenson, and F. Ayazi, "Electrical characterization of ald-coated silicon dioxide micro-hemispherical shell resonators," in *27th MEMS*. IEEE, 2014, pp. 612–615.

[17] D. Saito, C. Yang, A. Heidari, H. Najar, L. Lin, and D. A. Horsley, "Batch-fabricated high q-factor microcrystalline diamond cylindrical resonator," in *28th MEMS*. IEEE, 2015, pp. 801–804.

[18] P. M. Polunin, Y. Yang, M. I. Dykman, T. W. Kenny, and S. W. Shaw, "Characterization of mems resonator nonlinearities using the ringdown response," *J. Microelectromech. Sys.*, vol. 25, no. 2, pp. 297–303, 2016.

[19] T. Nagourney, J. Y. Cho, B. Shiari, A. Darvishian, and

K. Najafi, “259 second ring-down time and 4.45 million quality factor in 5.5 khz fused silica birdbath shell resonator,” in *19th TRANSDUCERS*. IEEE, 2017, pp. 790–793.

[20] J. Giner, D. Maeda, K. Ono, A. M. Shkel, and T. Sekiguchi, “Mems gyroscope with concentrated springs suspensions demonstrating single digit frequency split and temperature robustness,” *J. Microelectromech. Sys.*, vol. 28, no. 1, pp. 25–35, 2018.

[21] K. J. Åström and B. Wittenmark, *Computer Controlled Systems: Theory and Design*, 3rd ed. Dover Publications, 2011.

[22] B. Ho and R. Kalman, “Efficient construction of linear state variable models from input/output functions,” *Regelungstechnik*, vol. 14, pp. 545–548, 1966.

[23] H. Zeiger and A. McEwen, “Approximate linear realizations of given dimension via Ho’s algorithm,” *IEEE Trans. Autom. Control*, vol. 19, no. 2, pp. 153–153, 1974.

[24] E. Jonckheere, “Principal component analysis of flexible systems–open-loop case,” *IEEE Trans. Autom. Control*, vol. 29, no. 12, pp. 1095–1097, December 1984.

[25] J. T. Broch, *Principles of Experimental Frequency Analysis*. Springer, Dordrecht, 1990.